Ultrasound Image Deconvolution Using Fundamental and Harmonic Images

Mohamad Hourani, Adrian Basarab, Denis Kouamé, Jean-Yves Tourneret

Ultrasound Image Deconvolution Using Fundamental and Harmonic Images

Mohamad Hourani, *Student Member, IEEE*, Adrian Basarab, *Senior Member, IEEE*, Denis Kouamé, *Senior Member, IEEE*, and Jean-Yves Tourneret, *Fellow, IEEE*

***Abstract*— Ultrasound (US) image restoration from radio frequency (RF) signals is generally addressed by deconvolution techniques mitigating the effect of the system point spread function (PSF). Most of the existing methods estimate the tissue reflectivity function (TRF) from the so-called fundamental US images, based on an image model assuming the linear US wave propagation. However, several human tissues or tissues with contrast agents have a nonlinear behavior when interacting with US waves leading to harmonic images. This work takes this nonlinearity into account in the context of TRF restoration, by considering both fundamental and harmonic RF signals. Starting from two observation models (for the fundamental and harmonic images), TRF estimation is expressed as the minimization of a cost function defined as the sum of two data fidelity terms and one sparsity-based regularization stabilizing the solution. The high attenuation with a depth of harmonic echoes is integrated into the direct model that relates the observed harmonic image to the TRF. The interest of the proposed method is shown through synthetic and *in vivo* results and compared with other restoration methods.**

***Index Terms*— Alternating direction method of multipliers (ADMM), blind deconvolution, harmonic ultrasonic imaging, optimization, tissue reflectivity restoration.**

I. Introduction

ULTRASOUND (US) imaging is one of the leading imaging modalities due to its low cost, high frame rate, nonionizing risk, and ease of use. The main principle of US imaging consists in sending acoustical waves with central frequency f_0 into a medium (tissue). While propagating, US waves are distorted due to their nonlinear interaction with the medium. In addition to the common fundamental echoes obtained at frequency f_0, this distortion generates backscattered echoes at harmonic frequencies. In general, the study of these harmonics is generally reduced to the second component at frequency $2f_0$ because of the limited bandwidth of the transducer and the low signal-to-noise ratio (SNR) of higher harmonics. The principle of US wave distortion creating harmonic images and an example of a beamformed US image containing both fundamental and harmonic frequencies are shown in Fig. 1.

In applications such as blood perfusion or tissue characterization, contrast agents are used, which reinforces nonlinear interactions and generates harmonic data [1], [2]. However, several existing studies have shown that particular tissues can naturally cause sufficient wave distortion to generate observable harmonics, called tissue harmonic imaging (THI) [3], [4]. In THI, raw US data contains both fundamental and harmonic components, which can be isolated to reconstruct fundamental or harmonic images (see Fig. 1). This separation can be done using beamforming techniques, such as pulse inversion and phase cancellation [5]. It can also be done using postprocessing techniques, such as system identification [6], [7] or linear filtering. In this work, linear bandpass filters are used for this separation due to their simplicity and the low-frequency overlap between the fundamental and harmonic components.

The spatial resolution, contrast, and SNR of US images are generally affected by the limited bandwidth of the imaging transducer. To mitigate these drawbacks, image reconstruction and restoration techniques (beamforming, speckle reduction, and deconvolution) exist and were shown to improve the US image analysis, for instance, in the applications requiring quantitative measurements for meddiagnosis ical [8].

This article focuses on US image deconvolution, which is known to allow axial and lateral resolutions to be enhanced. The principle of US image deconvolution is to mitigate, via appropriate postprocessing, the effect of the imaging system impulse response, also called point spread function (PSF), which affects the spatial resolution of the image as a low-pass or bandpass filter. Depending on the available information about the PSF, deconvolution methods are usually referred to as nonblind, myopic [9]–[11], or blind methods [12], [13]. The main objective of this work is to show that combining harmonic and fundamental radio frequency (RF) data in a deconvolution problem can highly improve the restoration of the US image. To the best of our knowledge, a few studies have been conducted in this area. A super-resolution approach was considered in [14] exploiting the results of independent deconvolution of fundamental and harmonic images. Instead of deconvolving the two images independently, we propose in this work a joint deconvolution of fundamental and harmonic images through the minimization of an appropriate cost

Manuscript received July 22, 2020; accepted September 27, 2020. Date of publication October 1, 2020; date of current version March 26, 2021. *(Corresponding author: Mohamad Hourani.)*

Mohamad Hourani and Jean-Yves Tourneret are with the University of Toulouse, IRIT/INP-ENSEEIHT/TéSA, 31071 Toulouse, France (e-mail: mohamad.hourani@irit.fr; jean-yves.tourneret@irit.fr).

Adrian Basarab and Denis Kouamé are with the University of Toulouse, IRIT, CNRS UMR 5505, F-31062 Toulouse, France (e-mail: adrian.basarab@irit.fr; denis.kouame@irit.fr).

Digital Object Identifier 10.1109/TUFFC.2020.3028166

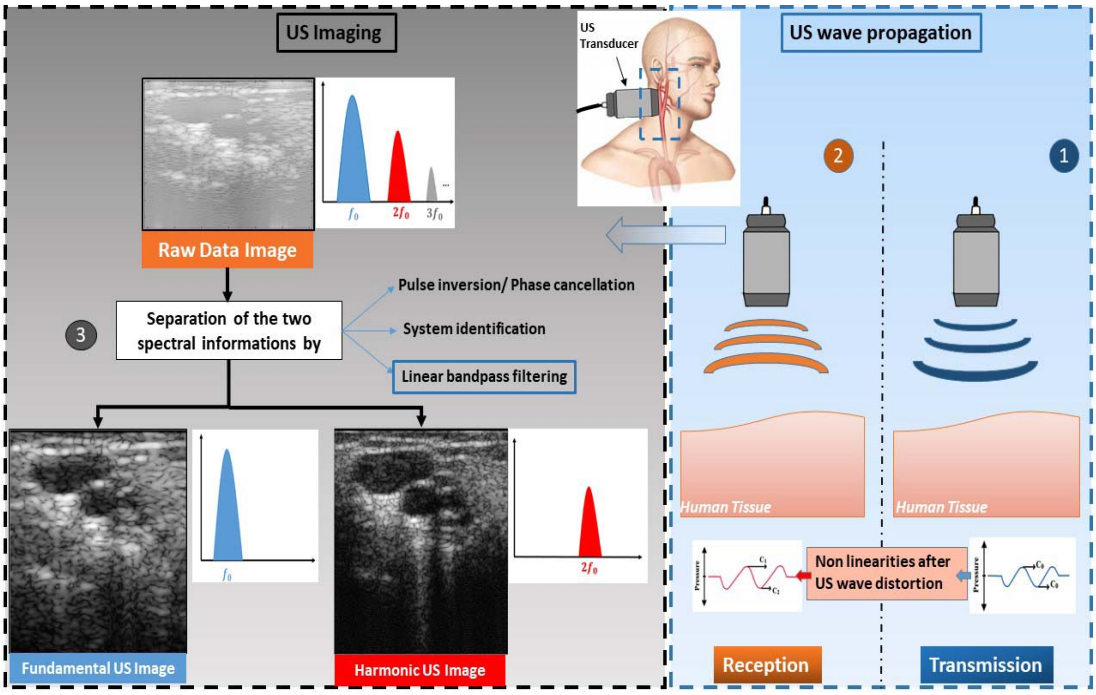

Fig. 1. Representation of pressure pulse distortion at the origin of harmonic US imaging and examples of fundamental and harmonic US images.

function. This cost function is composed of two quadratic data fidelity terms and one regularization. The data fidelity terms are constructed from the fundamental and harmonic image formation models using the unknown PSF. The existing algorithms for PSF estimation are based on parametric models [15] or estimate the PSF directly from the RF data [10]. This work considers the estimation of the PSF in a preprocessing step from the beamformed RF images followed by the estimation of the tissue reflectivity function (TRF) using an inverse problem. The proposed method is generic with respect to the acquisition scheme, which can be conventional focused or synthetic, i.e., with plane or diverging wave imaging. The results reported in this article have been obtained using RF images beamformed with the classical delay and sum approach, which is applied to raw data acquired using the standard pulse-echo imaging sequence.

The remainder of this article is organized as follows. Section II introduces the adopted US image formation models. Section III describes the proposed restoration algorithm, including PSF estimation. Section IV discusses synthetic data generation and experimental data acquisition. Results are presented in Section V, whereas conclusions and perspectives are reported in Section VI.

II. US Image Formation

Several methods have been introduced in the literature to model and solve the linear and nonlinear US wave propagation equation starting from the full-wave propagation model.

In the case of linear propagation, a US imaging model based on the spatial impulse response approach has been investigated in [16]–[18]. This model expresses the US RF signal as a convolution between a spatially varying PSF and the TRF. Interestingly, a similar model can also be considered in the case of nonlinear propagation with small nonlinearities [17], [18]. Specifically, the first-order Born approximation was investigated in [19], meaning that a single scattering phenomenon was considered in the wave propagation equation. As a consequence, the contribution of each scatterer in the imaged field was considered to be independent of the other scatterers, i.e., multiple scattering was ignored due to its reduced impact. Note that this assumption also holds in THI, given that the scattering of soft tissues is weak.

To further reduce the complexity of the restoration problem resulting from a spatially varying PSF [20], [21] and to maintain realistic conditions, most of the existing studies have addressed the restoration problem with a spatially invariant PSF by restricting the process to small image segments [22]–[25]. The proposed work follows this trend by considering a spatially invariant PSF. However, in contrast to most of the existing works, linear and nonlinear propagation models are jointly considered for TRF restoration. After forming the fundamental and harmonic images by filtering the beamformed RF image (more details about the filtering process are given in Section IV-B), the following image formation models are considered:

$$\boldsymbol{y}_f = \boldsymbol{H}_f \boldsymbol{r} + \boldsymbol{n}_f \tag{1}$$

$$\boldsymbol{y}_h = \boldsymbol{W}\boldsymbol{H}_h \boldsymbol{r} + \boldsymbol{n}_h, \tag{2}$$

where $\boldsymbol{y}_f$ and $\boldsymbol{y}_h \in \mathbb{R}^N$ are the observed fundamental and harmonic RF images, N is the number of image pixels, $\boldsymbol{r} \in \mathbb{R}^N$ is the TRF to be estimated, and $\boldsymbol{n}_f$ and $\boldsymbol{n}_h \in \mathbb{R}^N$ are white Gaussian additive noises. Moreover, the matrices $\boldsymbol{H}_f$ and $\boldsymbol{H}_h \in \mathbb{R}^{N\times N}$ are block circulant with circulant blocks (BCCB) matrices formed using the fundamental and harmonic PSFs $\boldsymbol{h}_f$ and $\boldsymbol{h}_h$. The attenuation of the harmonic image with depth

is considered in the second model by using a diagonal matrix $\boldsymbol{W} \in \mathbb{R}^{N\times N}$ that accounts for the level of attenuation at each depth. This attenuation can be adjusted using the ratio between the energies of the fundamental and first-harmonic spectra. The choice of this matrix will be explained in the section devoted to simulation results.

The proposed restoration problem consists in estimating the TRF $\boldsymbol{r}$ from the measurements $\boldsymbol{y_f}$ and $\boldsymbol{y_h}$. Note that the models in (1) and (2) also depend on the fundamental and harmonic PSFs that are unknown in practical situations. The estimation of the TRF $\boldsymbol{r}$ and the unknown PSFs $\boldsymbol{H}_f$ and $\boldsymbol{H}_h$ is detailed in Section III.

III. Two-Step Blind Deconvolution Algorithm

A. TRF Estimation With a Known PSF

This section introduces the algorithm proposed to estimate the TRF from fundamental and harmonic RF images based on the direct models (1) and (2), for a known PSF and a known weight matrix $\boldsymbol{W}$. From a Bayesian perspective, the TRF can be estimated using the standard maximum *a posteriori* (MAP) estimator, which maximizes the posterior distribution of the TRF defined

$$p(\boldsymbol{r}|\boldsymbol{y}_f, \boldsymbol{y}_h) \propto p(\boldsymbol{y}_f|\boldsymbol{r})\, p(\boldsymbol{y}_h|\boldsymbol{r})\, p(\boldsymbol{r}) \tag{3}$$

where $\propto$ means "proportional to" and $p(\boldsymbol{r})$ is the prior of $\boldsymbol{r}$, and the likelihood functions $p(\boldsymbol{y}_f|\boldsymbol{r})$ and $p(\boldsymbol{y}_h|\boldsymbol{r})$ are those of the following Gaussian distributions:

$$\begin{aligned} \boldsymbol{y}_f|\boldsymbol{r} &\sim \mathcal{N}(\boldsymbol{H}_f\boldsymbol{r}, \sigma_f^2\mathbf{I}_N) \\ \boldsymbol{y}_h|\boldsymbol{r} &\sim \mathcal{N}(\boldsymbol{W}\boldsymbol{H}_h\boldsymbol{r}, \sigma_h^2\mathbf{I}_N) \end{aligned} \tag{4}$$

where $\mathbf{I}_N$ is the $N\times N$ identity matrix, σ_f^2 and σ_h^2 are the noise variances, and $\mathcal{N}$ stands for the Gaussian distribution, and the two additive noises $\boldsymbol{n}_f$ and $\boldsymbol{n}_h$ are assumed to be independent. The negative log posterior of $\boldsymbol{r}$ is given by

$$\begin{aligned} -\log p(\boldsymbol{r}|\boldsymbol{y}_f, \boldsymbol{y}_h) \propto\ & \underbrace{\frac{1}{2}\|\boldsymbol{y}_f - \boldsymbol{H}_f\boldsymbol{r}\|^2}_{\text{Fundamental data fidelity term}} \\ & + \underbrace{\frac{1}{2}\|\boldsymbol{y}_h - \boldsymbol{W}\boldsymbol{H}_h\boldsymbol{r}\|^2}_{\text{Harmonic data fidelity term}} + \underbrace{\log[p(\boldsymbol{r})]}_{\text{Regularization}}. \end{aligned} \tag{5}$$

In this work, we consider a Laplacian prior distribution $p(\boldsymbol{r})$, leading to an ℓ_1-norm regularization term. This prior has been successfully used for US imaging in [12] and [25]–[27]. Finally, the TRF image $\boldsymbol{r}$ is estimated by solving the following minimization problem:

$$\boldsymbol{r}^* = \underset{\boldsymbol{r}}{\operatorname{argmin}} \frac{1}{2}\|\boldsymbol{y}_f - \boldsymbol{H}_f\boldsymbol{r}\|_2^2 + \frac{1}{2}\|\boldsymbol{y}_h - \boldsymbol{W}\boldsymbol{H}_h\boldsymbol{r}\|_2^2 + \mu\|\boldsymbol{r}\|_1 \tag{6}$$

where μ is a hyperparameter weighting the contribution of the sparse regularization with respect to the two data fidelity terms. The cost function in (6) is convex but nondifferentiable because of the ℓ_1-norm, thus preventing the use of traditional gradient-based algorithms. As an alternative, variable splitting-based algorithms developed for nondifferential problems, such as the alternating direction method of multipliers (ADMM) [28], the forward–backward algorithm (FBA) [29], or the fast iterative shrinkage thresholding algorithm (FISTA) [30], can be used to solve (6). This article proposes to estimate the TRF from fundamental and harmonic RF images using a dedicated algorithm based on ADMM [28], [31]. The main motivation for using ADMM is to split the optimization problem in (6) into several subproblems that are easy to solve, as shown hereafter [32], [33]. ADMM is a general optimization framework adapted to solve the following problem:

$$\begin{aligned} &\min_{u,v}\ f_1(\boldsymbol{u}) + f_2(\boldsymbol{v}) \\ &\text{s.t. } \boldsymbol{A}\boldsymbol{u} + \boldsymbol{B}\boldsymbol{v} = \boldsymbol{c} \end{aligned} \tag{7}$$

where f_1 and f_2 are closed convex and separable functions (depending on $\boldsymbol{u}$ and $\boldsymbol{v}$, respectively). The ADMM algorithm is based on the augmented Lagrangian $\mathcal{L}_A$ defined as

$$\mathcal{L}_A(\boldsymbol{u}, \boldsymbol{v}, \boldsymbol{\lambda}) = f_1(\boldsymbol{u}) + f_2(\boldsymbol{v}) + \frac{\beta}{2}\|A\boldsymbol{u} + B\boldsymbol{v} + \frac{\boldsymbol{\lambda}}{\beta}\|_2^2 \tag{8}$$

where β is a regularization parameter for the linear constraint and $\boldsymbol{\lambda}$ is the vector of Lagrangian multipliers. The vectors $\boldsymbol{u}$, $\boldsymbol{v}$ and $\boldsymbol{\lambda}$ are then computed as follows [28]:

$$\begin{aligned} &\text{For } k = 0, \ldots \\ &\quad \boldsymbol{u}^{k+1} = \operatorname{argmin}_{\boldsymbol{u}} \mathcal{L}_A(\boldsymbol{u}, \boldsymbol{v}^{(k)}, \boldsymbol{\lambda}^{(k)}) \\ &\quad \boldsymbol{v}^{k+1} = \operatorname{argmin}_{\boldsymbol{v}} \mathcal{L}_A(\boldsymbol{u}^{(k+1)}, \boldsymbol{v}, \boldsymbol{\lambda}^{(k)}) \\ &\quad \boldsymbol{\lambda}^{(k+1)} = \boldsymbol{\lambda}^{(k)} + \beta(\boldsymbol{A}\boldsymbol{u}^{(k+1)} + \boldsymbol{B}\boldsymbol{v}^{(k+1)} - \boldsymbol{c}). \end{aligned} \tag{9}$$

In order to solve (6) using the ADMM framework, we rewrite (6) as follows:

$$\begin{aligned} (\boldsymbol{u}^*, \boldsymbol{w}^*, \boldsymbol{z}^*) = \underset{\boldsymbol{u},\boldsymbol{w},\boldsymbol{z}}{\arg\min} & \frac{1}{2}\|\boldsymbol{y}_f - \boldsymbol{H}_f\boldsymbol{u}\|_2^2 \\ & + \frac{1}{2}\|\boldsymbol{y}_h - \boldsymbol{W}\boldsymbol{z}\|_2^2 + \mu\|\boldsymbol{w}\|_1 \end{aligned} \tag{10}$$

with

$$\begin{cases} f_1(\boldsymbol{u}) = \frac{1}{2}\|\boldsymbol{y}_f - \boldsymbol{H}_f\boldsymbol{u}\|_2^2 \\ f_2(\boldsymbol{v}) = \frac{1}{2}\|\boldsymbol{y}_h - \boldsymbol{W}\boldsymbol{z}\|_2^2 + \mu\|\boldsymbol{w}\|_1 \\ \boldsymbol{z} = \boldsymbol{H}_h\boldsymbol{r}, \boldsymbol{w} = \boldsymbol{u} = \boldsymbol{r} \\ \boldsymbol{v} = \begin{bmatrix} \boldsymbol{w} \\ \boldsymbol{z} \end{bmatrix} \end{cases}$$

$$\text{and} \begin{cases} \boldsymbol{A} = \begin{bmatrix} I_N \\ \boldsymbol{H}_h \end{bmatrix} \\ \boldsymbol{B} = \begin{bmatrix} -I_N & 0 \\ 0 & -I_N \end{bmatrix} \\ \boldsymbol{c} = \mathbf{0}_{2N} \end{cases}.$$

The main motivation behind the proposed parameterization, and in particular the use of the auxiliary variables $\boldsymbol{u}$ and $\boldsymbol{v}$, is to separate the operators $\boldsymbol{W}$ and $\boldsymbol{H_h}$. As it will be shown next, $\boldsymbol{H_h}$ can be diagonalized in the Fourier domain due to its BCCB property, whereas $\boldsymbol{W}$ is a diagonal matrix in the spatial domain. Separating $\boldsymbol{H_h}$ and $\boldsymbol{W}$ simplifies the optimization algorithm, which can be divided into two easier subproblems

in the Fourier domain (for $\boldsymbol{H_h}$) and the spatial domain (for $\boldsymbol{W}$), where these two matrices have diagonal representations.

The solution of (10) can be iteratively obtained in the ADMM framework as described in Algorithm 1 and further detailed in the following three main steps. Note that the algorithm is initialized by setting $\boldsymbol{u}^{(0)}$, $\boldsymbol{z}^{(0)}$) and $\boldsymbol{w}^{(0)}$) to the fundamental image and the Lagrangian multipliers $\boldsymbol{\lambda}^{(0)}$) to 0.

Algorithm 1 ADMM Algorithm for TRF Estimation

Input: $\boldsymbol{y}_f$, $\boldsymbol{y}_h$, $\boldsymbol{H}_f$, $\boldsymbol{H}_h$.

1. Set $k = 0$, choose $\mu > 0$, $\beta > 0$, u^0, v^0, λ^0
2. Repeat until the relative cost function error $< \epsilon$

// *Estimate* $\boldsymbol{u}$ *(closed-form solution in the Fourier domain)*

3. $\boldsymbol{u^{k+1}} = \min_{u} \frac{1}{2}\|\boldsymbol{y}_f - \boldsymbol{H}_f\boldsymbol{u}\|_2^2 + \frac{\beta}{2}\|A\boldsymbol{u} + B\boldsymbol{v^k} + \frac{\boldsymbol{\lambda}^k}{\beta}\|_2^2$

// *Estimate* $\boldsymbol{v} = [\begin{matrix}\boldsymbol{w}\\ \boldsymbol{z}\end{matrix}]$

// *Estimate* $\boldsymbol{w}$ *using soft thresholding*

4. $\boldsymbol{w^{k+1}} = \min_{\boldsymbol{w}} \ \mu\|\boldsymbol{w}\|_1 + \frac{\beta}{2}\|\boldsymbol{u^{k+1}} - \boldsymbol{w} + \frac{\boldsymbol{\lambda_1^k}}{\beta}\|_2^2$

// *Estimate* $\boldsymbol{z}$ *(closed-form solution in the Fourier domain)*

5. $\boldsymbol{z^{k+1}} = \min_{z} \ \frac{1}{2}\|\boldsymbol{y}_h - W\boldsymbol{z}\|_2^2 + \frac{\beta}{2}\|\boldsymbol{H}_h\boldsymbol{u^{k+1}} - \boldsymbol{z} + \frac{\boldsymbol{\lambda_2^k}}{\beta}\|_2^2$

// *Update the Lagrangian multiplier*

6. $\boldsymbol{\lambda^{k+1}} = \boldsymbol{\lambda}^k + \beta(\boldsymbol{Au^{k+1}} + \boldsymbol{Bv^{k+1}})$

Step 1: Update $\boldsymbol{u}$ using the analytical solution of the optimization problem in line 3 of Algorithm 1. Denoting as

$$\boldsymbol{\lambda} = \begin{bmatrix}\boldsymbol{\lambda_1}\\ \boldsymbol{\lambda_2}\end{bmatrix} \in \mathbb{R}^{2\ N}$$

the vector of Lagrangian multipliers, the update of $\boldsymbol{u}$ at iteration k is defined as

$$\begin{aligned}\boldsymbol{u}^{k+1} = &\left(\boldsymbol{H}_f^T\boldsymbol{H}_f + \beta\boldsymbol{H}_h^T\boldsymbol{H}_h + \beta\boldsymbol{I}_N\right)^{-1}\boldsymbol{z}^k\\ &\times\left(\boldsymbol{H}_f^T y_f + \beta\boldsymbol{H}_h^T - \boldsymbol{\lambda_1}^k\right.\\ &\left.-\boldsymbol{H}_h^T\boldsymbol{\lambda_2}^k + \beta\boldsymbol{w}^k\right).\end{aligned} \tag{11}$$

Under the hypothesis of circular convolution, $\boldsymbol{H}_f$ and $\boldsymbol{H}_h$ are BCCB matrices having the spectral decompositions

$$\boldsymbol{H}_f = \boldsymbol{F}^*\boldsymbol{\Lambda}_f\boldsymbol{F} \tag{12}$$

$$\boldsymbol{H}_h = \boldsymbol{F}^*\boldsymbol{\Lambda}_h\boldsymbol{F} \tag{13}$$

where $\boldsymbol{F}$ and $\boldsymbol{F}^*$ are the 2-D Fourier and inverse Fourier transform matrices and $\boldsymbol{\Lambda}_f = \text{diag}(\boldsymbol{Fh}_f)$ and $\boldsymbol{\Lambda}_h = \text{diag}(\boldsymbol{Fh}_h)$ are diagonal matrices whose diagonal elements are the Fourier coefficients of the first column of matrices $\boldsymbol{H}_f$ and $\boldsymbol{H}_h$. The solution of (11) can finally be written as follows:

$$\begin{aligned}\boldsymbol{u}^{k+1} = &\boldsymbol{F}^*\left(\boldsymbol{\Lambda}_f^*\boldsymbol{\Lambda}_f + \beta\boldsymbol{\Lambda}_h^*\boldsymbol{\Lambda}_h + \beta\boldsymbol{I}_N\right)^{-1}\\ &\times\left(\boldsymbol{\Lambda}_f^*\boldsymbol{F}y_f + \beta\boldsymbol{\Lambda}_f^*\boldsymbol{F}\boldsymbol{z}^k - \boldsymbol{F}\boldsymbol{\lambda}_1^k - \boldsymbol{\Lambda}_f^*\boldsymbol{F}\boldsymbol{\lambda_2}^k + \beta\boldsymbol{F}\boldsymbol{w}^k\right).\end{aligned} \tag{14}$$

The computational complexity of the solution is reduced from $\mathcal{O}(N^3)$ in (11) to $\mathcal{O}(N\log N)$ in (14) [using the decompositions in (12) and (13)]. In (14), $\boldsymbol{\Lambda}_f^*\boldsymbol{\Lambda}_f$ and the Fourier operator can be computed with complexities of the order $\mathcal{O}(N)$ and $\mathcal{O}(N\log N)$.

Step 2: $\boldsymbol{v} = [\begin{matrix}\boldsymbol{w}\\ \boldsymbol{z}\end{matrix}]$ is updated using two substeps.

Substep 2.1: Update $\boldsymbol{w}$ by minimizing the cost function in line 4 of Algorithm 1. The solution to this problem can be simply implemented by a soft-thresholding operator [34]

$$\begin{aligned}\boldsymbol{t}^k &= \boldsymbol{u}^{k+1} + \boldsymbol{\lambda}_1^k/\beta\\ \boldsymbol{w}^{k+1} &= \text{soft}_{\frac{\mu}{\beta}}(\boldsymbol{t}^k) = \max\left\{|\boldsymbol{t}^k| - \frac{\mu}{\beta}, 0\right\}\text{sign}(\boldsymbol{t}^k).\end{aligned} \tag{15}$$

Substep 2.2: The optimization problem in line 5 of Algorithm 1 has an analytical solution defined as

$$\boldsymbol{z}^{k+1} = \left(\boldsymbol{W}^T\boldsymbol{W} + \beta\boldsymbol{I}_N\right)^{-1}\left(\boldsymbol{W}^T\boldsymbol{y}_h + \beta\boldsymbol{H}_h\boldsymbol{u}^{k+1} + \boldsymbol{\lambda}_2^k\right). \tag{16}$$

Step 3: Update the Lagrange multiplier as suggested in [28]

$$\boldsymbol{\lambda}^{k+1} = \boldsymbol{\lambda}^k + \beta\left(\boldsymbol{Au}^{k+1} + \boldsymbol{Bv}^{k+1}\right). \tag{17}$$

As shown in Algorithm 1, the proposed ADMM-based algorithm iterates the previous steps until a stopping criterion has been satisfied. The stopping criterion for all the results reported in this article was the relative error between two consecutive values of the cost function in (10). The tolerance parameter ϵ was set to 10^{-4}.

B. PSF Estimation

The TRF estimation algorithm proposed in Section III-A assumed the knowledge of the fundamental and harmonic PSFs.

These PSFs can be estimated from the data, i.e., from the beamformed RF images that are also used for TRF restoration. Several parametric approaches have been investigated for this estimation, exploiting an *a priori* model of the PSF (see [10], [15], [35]). To overcome the rigidity of parametric models, several nonparametric methods can also be found in the literature, among which one may cite the homomorphic technique [36]–[38]. The homomorphic method assumes that the PSF and the TRF have disjoint supports in the cepstrum domain and, thus, estimate the amplitude of the PSF by low-pass filtering. Application of the homomorphic filtering to US image restoration has been studied in [9] and [10] in. The basic idea of this method is to rewrite the convolution model (2) such that the PSFs and the TRF are separable. More precisely, a generic noiseless convolution model ($\boldsymbol{y}(x) = \boldsymbol{h}(x) \otimes \boldsymbol{r}(x)$) (where $\boldsymbol{y}$, $\boldsymbol{h}$, and $\boldsymbol{r}$ represent the RF data, PSF and TRF, respectively) can be expressed in the spectral domain as

$$Y(\omega) = H(\omega)R(\omega) \tag{18}$$

where $Y(\omega)$, $H(\omega)$, and $R(\omega)$ are the Fourier transform of $y(x)$, $h(x)$, and $r(x)$, respectively, ω is the frequency variable, and x is the location in the spatial domain, and the noise

has been ignored by simplicity. The complex logarithmic transformation of $Y(\omega)$ is thus defined as

$$\log|Y(\omega)| = \log|H(\omega)| + \log|R(\omega)|, \tag{19}$$

$$\angle Y(\omega) = \angle H(\omega) + \angle R(\omega) \tag{20}$$

where the symbols $|.|$ and $\angle$ denote the magnitude and the phase of the complex function, respectively. The goal of the homomorphic methods is to discriminate the PSF and the TRF terms based on their smoothness properties. The PSF function is usually smooth in contrast to the reflectivity function that can be considered as noise. Despite its efficiency, the homomorphic filter suffers from its inability to estimate the PSF phase. The minimum phase assumption can then be used to build a robust solution for the proposed deconvolution problem. More precisely, the adopted strategy applies a phase unwrapping step and subsequently uses a smoothing procedure as in [10]. Note that the PSF estimation algorithm is independently applied to fundamental and harmonic RF images, after separation by bandpass filtering. An outlier removal step introduced in [10] is also used in order to build an outlier resistant decomposition. The threshold for outlier removal was set to 1. Note that the algorithm implicitly applies a denoising step since some of the wavelet coefficients are set to zero by the thresholding operation. These coefficients belong to a finer wavelet decomposition level (here, wavelets of Daubechies with two vanishing moments were used, and the decomposition level was set to be 3). Finally, the estimation of the PSF was done from a region of interest (ROI) extracted around the TX focal point, in order to benefit from optimal SNR conditions. Note that a detailed analysis of the sensitivity of US deconvolution to PSF parameters can be found in [39].

IV. Data and Evaluation Metrics

A. Data Simulation and Acquisition

1) Synthetic Data: A controlled ground-truth TRF was computed from a kidney magnetic resonance image (MRI) slice, by generating 10^6 scatterers (i.e., 30 scatterers per resolution cell) with random Gaussian amplitudes. The gray levels of the MRI image pixels were used to scale the variance of the Gaussian distribution. The size of the resulting TRF image is 1150×300 pixels. Fundamental ($\boldsymbol{y}_f$) and harmonic ($\boldsymbol{y}_h$) RF images were simulated by convolving this TRF with two spatially invariant PSFs $\boldsymbol{h}_f$ and $\boldsymbol{h}_h$, with central frequencies $f_0 = 3.5$ MHz and $2f_0 = 7$ MHz. The two PSFs were generated based on a simple Gaussian window modulated by a sine function. The full-width at half-maximum (FWHM) of the fundamental PSF was 3 mm in the lateral direction and 1.1 mm in the axial direction. The FWHM of the harmonic PSF was 1 mm in the lateral direction and 0.5 mm in the axial direction. Both PSFs were generated using six sine cycles. The resulting images were contaminated by additive white Gaussian noise corresponding to an SNR = 40 dB. The harmonic image was finally generated by including an attenuation matrix $\boldsymbol{W}$, accounting for the loss of wave amplitude due to absorption and scattering, to respect the direct model introduced in Section II. More precisely, the simulation of $\boldsymbol{W}$ was inspired by the exponential attenuation model used in US imaging defined by

$$A(z) = A_0 e^{-\mu_A z} \tag{21}$$

where $A(z)$ is the signal amplitude at a given depth z, A_0 is the initial signal amplitude, and μ_A is the attenuation factor, fixed to 1.15 Nepers/cm. Note that this model assumes that the attenuation only depends on the depth and is thus constant with respect to the lateral direction.

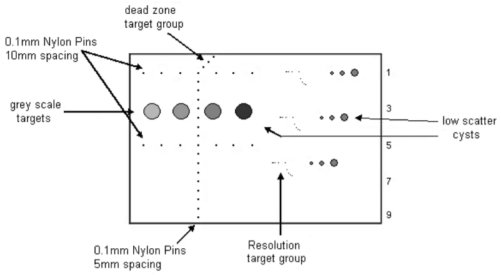

Fig. 2. Phantom model 404GS LE, Gammex Inc.

To further consider nonlinear propagation effects, a second synthetic RF image was generated using a nonlinear US image simulator called CREANUIS [44]. The objective of this second simulated image was to account for more realistic simulations and to evaluate the interest of the proposed method for short excitation pulses. In particular, a linear probe with a 245-μm pitch and 30-μm kerf was simulated. In transmission, 64 elements were activated, focused at 30 mm depth, and apodized with a Hanning window. The TX signal was a one-cycle sine burst at 3 MHz with Gaussian tapering. The TRF corresponded to the fetus example available in Field II [46]. The attenuation coefficient B/A was fixed at 3.5.

2) Experimental Images: The experimental data were acquired with a ULA-OP 256 research scanner connected to the wideband 192-element linear array probe LA533 (Esaote S.p.A., Florence, Italy), with 110% bandwidth centered at 8 MHz and a 245-μm pitch. In transmission (TX), 64 elements were activated, focused at 33 mm depth, and apodized with a Hanning window with an F-number equal to 4. The TX excitation signal was a ten-cycle sine burst at 5 MHz with the Hanning tapering and peak amplitude of 90 Vpp, for all the performed scans [40]. The size of the RF images is 384×4480, i.e., there are 384 scanned RF lines and the number of samples covering the depth of 45 mm is 4480. The sampling frequency was 78.125 MHz. Two acquisitions were considered to test the proposed algorithms, as described hereafter.

a) Phantom image: The first data were acquired on a tissue-mimicking phantom (model 404GS LE, Gammex Inc., Middleton, WI, USA), including both anechoic/hypoechoic cysts and wire targets, as shown in Fig. 2. The simple structures in this phantom allowed us to objectively evaluate the resolution and the contrast gain enabled by the proposed method.

b) Carotid image: The second acquisition was done *in vivo* by scanning the carotid artery and jugular vein of a young

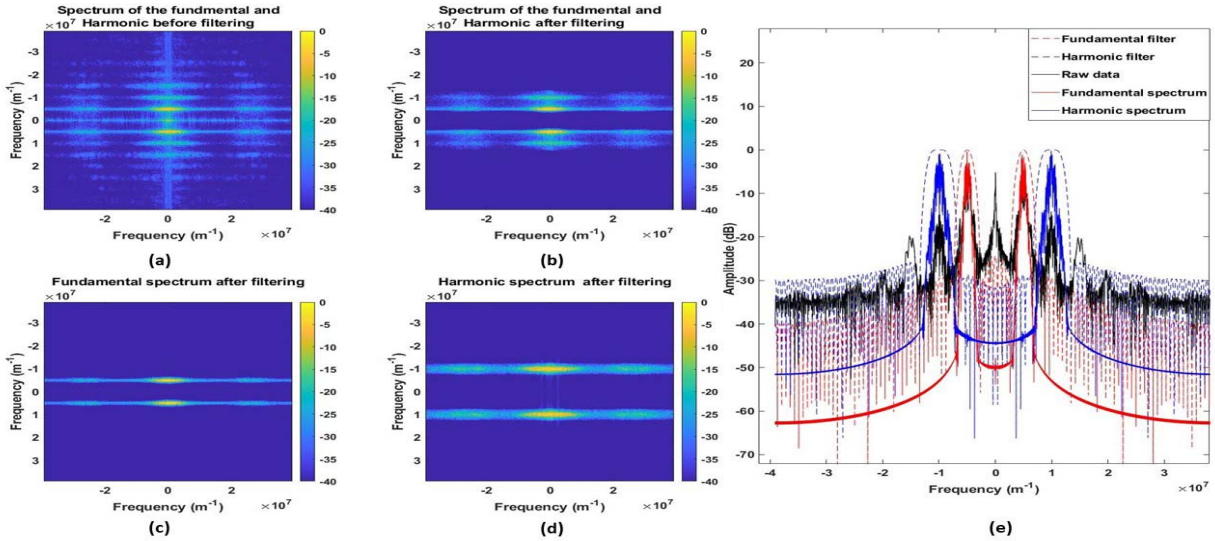

Fig. 3. Carotid image. (a) Spectrum of the original RF image. (b) Spectrum of the filtered RF image containing the mixed information from fundamental and harmonic data. (c) Spectrum of the fundamental image $\boldsymbol{y}_f$ after filtering. (d) Spectrum of the harmonic image $\boldsymbol{y}_h$ after filtering. (e) Spectrum of one RF line highlighting the fundamental and first-harmonic filtering.

healthy volunteer. This image contains more complicated structures and represents a more difficult challenge than the previous phantom to prove the functionality of the proposed restoration procedure.

B. Spectral Analysis of the Experimental Data

This section provides an analysis of the experimental data in the Fourier domain. This analysis has mainly two objectives: 1) justify the separation of fundamental and harmonic images by linear filtering and 2) explain how the attenuation matrix $\boldsymbol{W}$ was estimated from real data.

In order to obtain the fundamental and harmonic images, a bandpass FIR filter with a Hamming window was applied to the RF image. The filter bandwidths for the fundamental and harmonic images were set to [4 MHz, 6 MHz] (order 50) and [9 MHz, 11 MHz] (order 60), respectively. These bandwidths are in agreement with the fundamental and first-harmonic frequencies of the transducer, i.e., $f_0 = 5$ MHz and $2f_0 = 10$ MHz. An example of the result obtained with this filtering procedure is shown in Fig. 3 for a carotid image. Note that there is a reduced spectral overlap between the fundamental and first-harmonic spectra, justifying the use of linear filtering for their separation.

In the case of experimental images, the attenuation matrix $\boldsymbol{W}$ was constructed directly from the observed data, without considering any *a priori* model. More precisely, we computed the ratios between the energies of the fundamental and harmonic components within sliding blocks extracted from the RF image at each depth [41]. An example of estimated weights obtained with this method is shown in Fig. 4.

C. Quantitative Metrics

To quantitatively evaluate the accuracy of the deconvolution results, five metrics were employed. Two of these metrics are only applied to the simulated data because they require the knowledge of the ground-truth TRF. The three other metrics are dedicated to experimental data, for which the true TRF is not available.

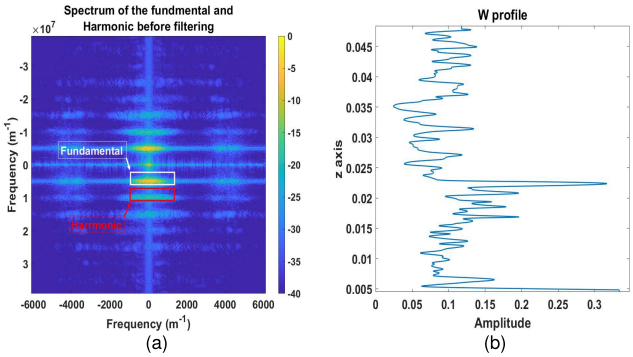

Fig. 4. Example of weights for the carotid image. (a) Regions used to compute the energies of the fundamental (red) and harmonic (blue) spectra. (b) Diagonal elements of $\boldsymbol{W}$ with respect to the axial direction.

The structural similarity (SSIM) is an image quality measure considering human visual perception defined as [42]

$$\text{SSIM} = \frac{(2\mu_x\mu_{\hat{x}} + c_1)(2\sigma_{x\hat{x}} + c_2)}{(\mu_x^2 + \mu_{\hat{x}}^2 + c_1)(\sigma_x^2 + \sigma_{\hat{x}}^2 + c_2)} \tag{22}$$

where μ_x, $\mu_{\hat{x}}$, σ_x, and $\sigma_{\hat{x}}$ are the means and standard deviations of the true image $\boldsymbol{x}$ and its reconstruction $\hat{\boldsymbol{x}}$ (obtained using restoration or beamforming) and $\sigma_{x\hat{x}}$ is the covariance between $\boldsymbol{x}$ and $\hat{\boldsymbol{x}}$. The values of c_1 and c_2 were set to the default values used in SSIM: $c_1 = (0.01 \times L)^2$ and $c_2 = (0.03 \times L)^2$, where L is the dynamic range. The root-mean-square error (RMSE) between a vectorized image $\boldsymbol{x}$ and its reconstruction $\hat{\boldsymbol{x}}$ (obtained using restoration or beamforming) is defined as

$$\text{RMSE} = \sqrt{\|\boldsymbol{x} - \hat{\boldsymbol{x}}\|_2^2}. \tag{23}$$

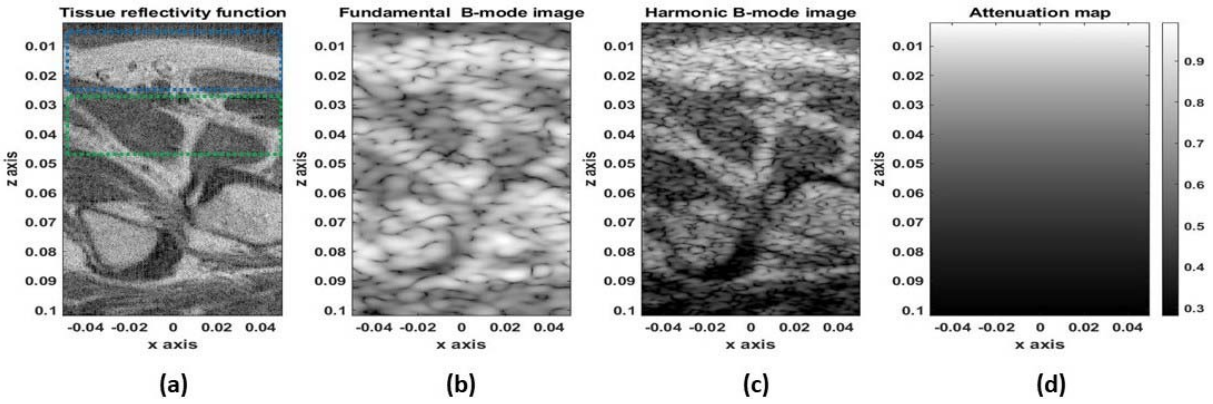

Fig. 5. (a) TRF mimicking a human kidney ($\boldsymbol{r}$ of size 1150 × 300 pixels). (b) Simulated fundamental image $\boldsymbol{y}_f$. (c) Simulated harmonic image $\boldsymbol{y}_h$. (d) Attenuation map used to simulate the harmonic image in (b), whose values are equal to 1 (no attenuation) close to the probe and to 0.3 (high attenuation) at the bottom of the image. Note that all the images are shown in B-mode for better visualization and with 60-dB dynamic range.

The contrast-to-noise ratio (CNR) defines the contrast level between two regions extracted from an image in dB

$$\mathrm{CNR} = 10\log_{10}\left(\frac{|\mu_1 - \mu_2|}{\sqrt{\sigma_1^2 + \sigma_2^2}}\right) \tag{24}$$

where μ_1 and μ_2 are the means of pixels located in the two defined regions and σ_1 and σ_2 are the standard deviations of these regions.

The resolution gain (RG) was measured based on the normalized autocorrelation function before and after deconvolution. The number of pixels of the normalized autocorrelation function having values higher than 0.75 (3 dB) was counted in the original and the deconvolved images. The RG is defined as the ratio between these two numbers, as suggested in [12].

V. Results and Discussion

The accuracy of the proposed restoration algorithm was evaluated and compared with two existing state-of-the-art methods. The first method consists in restoring the TRF from the fundamental RF image only, without accounting for the first-harmonic data. This approach (referred to as "LASSO-fundamental") estimates the TRF by minimizing the following LASSO-type cost function [14], [18]:

$$\min_{\boldsymbol{r}} \frac{1}{2}\|\boldsymbol{y}_f - \boldsymbol{H}_f\boldsymbol{r}\|_2^2 + \mu\|\boldsymbol{r}\|_1. \tag{25}$$

Note that similar to the proposed algorithms, the ℓ_1-norm regularization is used in order to allow a fair comparison.

The second approach takes into consideration both fundamental and harmonic RF images as in [14]. It sums the TRF estimated by (25) and the TRF estimated from the harmonic RF image using the following problem:

$$\min_{\boldsymbol{r}} \frac{1}{2}\|\boldsymbol{y}_h - \boldsymbol{H}_h\boldsymbol{r}\|_2^2 + \mu\|\boldsymbol{r}\|_1. \tag{26}$$

The final RF estimator (referred to as "LASSO-sum" in this work and as compounded estimator in [14]) is obtained by pixelwise summation of the two restored TRFs, normalized such that the pixels of the final TRF sums to 1.

TABLE I
Quantitative Results Corresponding to the Images Fig. 6(b)–(e). The CNR Is Computed With Respect to the Rectangular Regions Shown in Fig. 5

	LASSO Fundamental	LASSO Harmonic	LASSO Sum	Proposed method
CNR (dB)	-0.931	-5.874	-0.857	**1.859**
SSIM (%)	47	53.2	55.35	**57.9**
RMSE	1.031	1.110	1.010	**0.685**
RG/fund	63	63	63	63
RG/har	25	25	25	25

Finally, the proposed approach will also be compared to an estimator based on (26) only, referred to as "LASSO-harmonic," in order to appreciate the interest of the harmonic image. Note that the LASSO problem is very common and can be solved using several optimization algorithms, as suggested in the literature [28], [43]. In order to obtain a fair comparison with the proposed algorithm, ADMM was also used to minimize the functions in (25) and (26).

A. Results on Synthetic Data

Two kinds of results are presented in this section to compare the proposed method with LASSO-fundamental, LASSO-harmonic, and LASSO-sum.

1) Supervised Approach: The first results are obtained in the ideal case of a known PSF, referred to as "supervised deconvolution." The simulated TRF and the corresponding fundamental and harmonic images are shown in Fig. 5(a)–(c). Fig. 5(d) shows the exponential attenuation map, used to simulate the harmonic image, which decays from 1 to 0.3 with the imaging depth following (21). The original and estimated TRFs obtained using the different methods are shown in Fig. 6. Zooms corresponding to the red rectangles are also shown in Fig. 6 for better visualization. The visual inspection of the TRF allows us to appreciate qualitatively the better accuracy of the proposed method in terms of contrast and resolution. A quantitative assessment is shown in Table I confirming the qualitative results. Note that the RG is computed both with respect to fundamental and harmonic images, defined as "RG/fund" and "RG/har." More specifically, the proposed

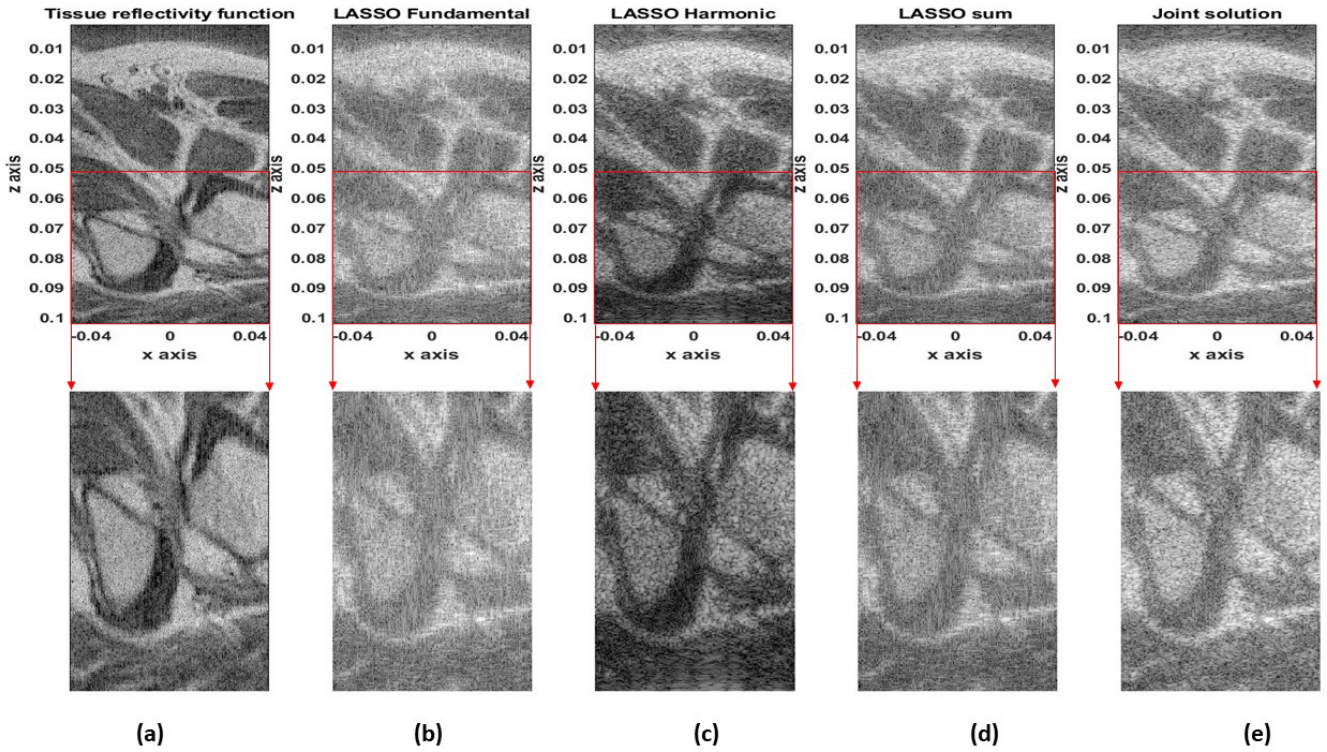

Fig. 6. (a) TRF mimicking a human kidney (r of size 1150 $\times$ 300 pixels), TRF estimated by (b) LASSO-fundamental, (c) LASSO-harmonic, (d) LASSO-sum, and (e) proposed method. All the estimated TRFs are obtained using a supervised approach, i.e., using the true PSF. Note that all the images are shown in B-mode for better visualization and with 60-dB dynamic range.

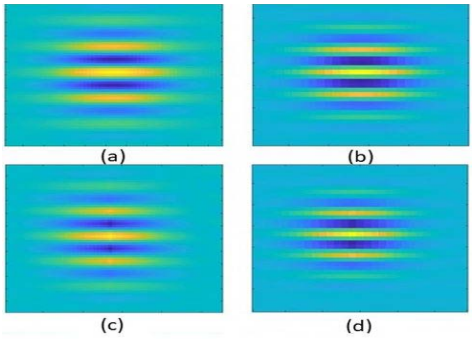

Fig. 7. Left column: fundamental PSF (a) true and (c) estimated by homomorphic filtering. Right column: harmonic PSF (b) true and (d) estimated by homomorphic filtering.

TABLE II
QUANTITATIVE RESULTS CORRESPONDING TO THE IMAGES OF FIG. 8

	LASSO Fundamental	LASSO Harmonic	LASSO Sum	Proposed method
CNR	3.067	3.061	3.231	**5.254**
SSIM (%)	43.63	44.15	40.05	**49.79**
RMSE	1.334	0.911	0.1309	**0.0783**
RG/fund	2.739	**9**	3.571	**9**
RG/har	1.087	**3.571**	2.027	**3.571**

TABLE III
QUANTITATIVE ASSESSMENT OF THE ESTIMATED PSF WITH RESPECT TO THE TRUE PSF

	PSF in Fig. 6(c)	PSF in Fig. 6(d)
SSIM	0.9976	0.9981
RMSE	0.1511	0.2022

method yields a good compromise between the good contrast of the fundamental image and the good spatial resolution of the harmonic image, with the ability of compensating the high harmonic attenuation with depth.

2) Two-Step Blind Deconvolution Approach: The proposed method is evaluated using two sets of synthetic data by estimating both PSFs and the TRF successively. This experiment estimates the PSFs using the fundamental and harmonic images through the homomorphic filtering detailed in [10]. This is performed prior to the TRF restoration process. The first set of data is obtained using the synthetic data of Section IV-A1. The results are shown in Fig. 8. One can observe that the deconvolution is less accurate than in the supervised case because the PSFs are estimated and not set to their true values. However, the proposed method provides very competitive results compared with the state of the art. Quantitative results corresponding to this experiment are shown in Table II, confirming the interest of the proposed method.

In order to investigate the efficiency of PSF estimation, the truly fundamental and harmonic PSF and the estimates obtained by the preprocessing (homomorphic filtering) step are shown in Fig. 7. Besides the visual assessment, Table III confirms a good similarity, in the sense of RMSE, between the actual PSF and its estimate.

The interest of the proposed method for short excitation pulses and in the presence of nonlinear propagation effects can be appreciated in Fig. 9 for an image simulated

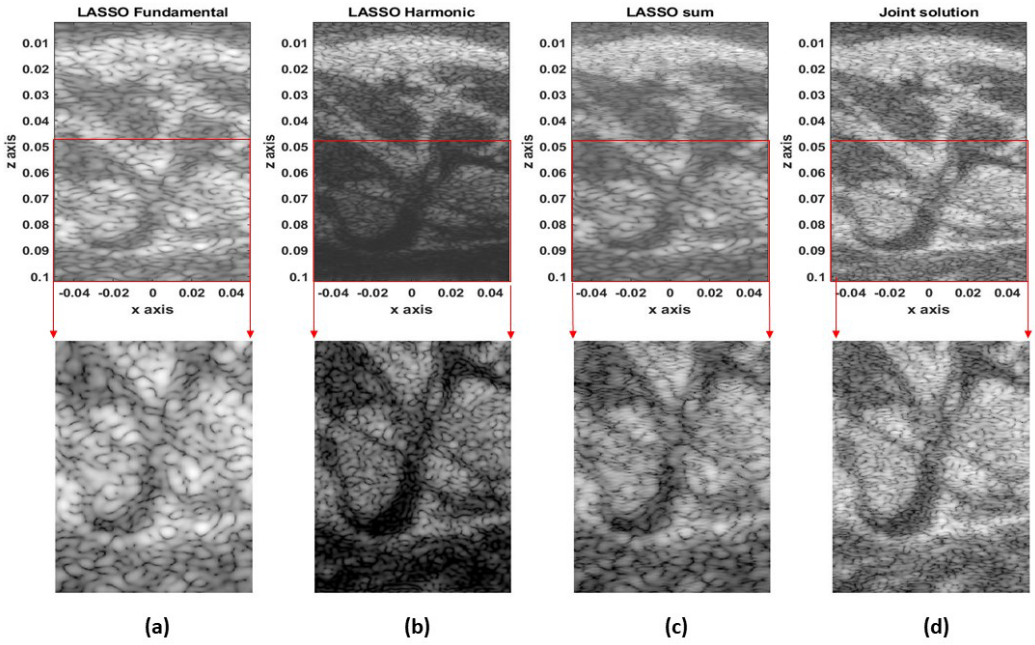

Fig. 8. Estimated TRF using a two-step approach with (a) LASSO-fundamental estimated from the fundamental image in Fig.5 (b), (b) LASSO-harmonic estimated from the harmonic image in Fig. 5(c), (c) LASSO-sum, and (d) proposed method. All the TRF were estimated using PSF preestimated by homomorphic filtering of the RF images. Note that all the images are shown in B-mode for better visualization and with 60-dB dynamic range.

TABLE IV
QUANTITATIVE RESULTS CORRESPONDING TO THE IMAGES OF FIG. 9

	LASSO Fundamental	**LASSO Harmonic**	**LASSO Sum**	**Proposed method**
CNR	12.162	**12.928**	12.388	12.617
RG/fund	1.235	2.333	1.909	**3**
RG/har	0.629	1.101	0.818	**1.286**

TABLE V
QUANTITATIVE RESULTS COMPUTED FROM THE IMAGES OF FIG. 10

	LASSO Fundamental	LASSO Harmonic	LASSO Sum	Proposed method
CNR	0.469	1.686	1.494	**2.417**
RG/fund	2.778	3.154	3.545	**6.231**
RG/har	2.231	2.333	2.231	**2.636**

with CREANUIS [44]. Results reported in Table IV confirm the visual interpretation; the proposed method yields the highest RG among all the restoration methods and the second-best CNR after LASSO-harmonic, which misses, however, the information in depth because of attenuation.

B. Results on Experimental Images

This section analyzes some results obtained using phantom and real carotid data. In contrast to the simulated data, the system PSFs are unknown in these scenarios and have to be estimated. Therefore, we investigate a PSF preestimation using homomorphic filtering followed by a TRF deconvolution.

1) Phantom Image Results: The fundamental and harmonic images associated with the considered phantom are shown in Fig. 10(a) and (b). The better spatial resolution enabled by harmonic images can be clearly observed by the wire responses. The attenuation of harmonic echoes is very low for this example. For this reason, the matrix $\boldsymbol{W}$ accounting for attenuation in the harmonic direct model was set to the identity matrix.

The results using the proposed approach and the different restoration methods are shown in Fig. 10(c)–(f). In general, all the restoration methods that consider the harmonic data (LASSO-harmonic, LASSO-sum, and proposed method) exhibit good spatial resolution. Furthermore, LASSO-sum and the proposed algorithm compensate for the harmonic attenuation at high depths by including information from the fundamental image, as shown in the zooms of Fig. 10. Cysts are also better defined in the restored images compared with the noisy images. To confirm these remarks, a plot extracted from the estimated TRF is shown in Fig. 11. The proposed method provides images with good spatial resolution, i.e., with a similar or better FWHM of the wire echo compared with harmonic and fundamental images.

The quantitative results are shown in Table V. They show on one hand the competitivity of the proposed method both in terms of contrast and spatial resolution and on the other hand that slightly better results are obtained, for all the methods, with the PSF estimated in a preprocessing step.

2) Carotid Results: The fundamental and harmonic carotid images are shown in Fig. 12(a) and (b). From these images, one can clearly observe the better spatial resolution of the harmonic image, at the cost of higher attenuation with depth compared with the fundamental image. In contrast to the phantom experiment, the attenuation matrix $\boldsymbol{W}$ was estimated, as explained in Section IV-B. This matrix has a crucial role in this data set, due to its ability to balance fundamental

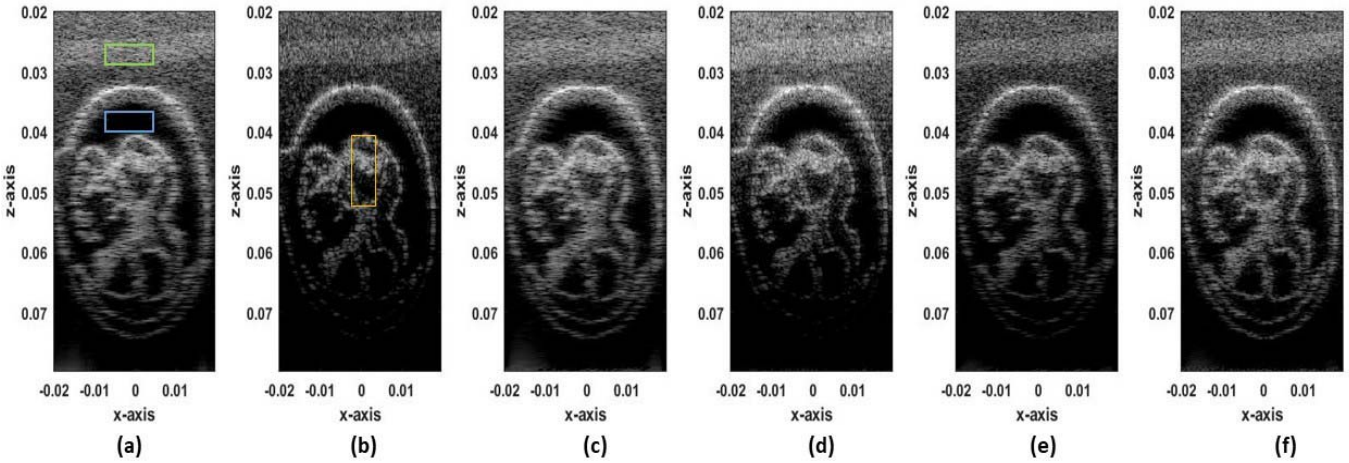

Fig. 9. Results on data simulated with CREANUIS. (a) Fundamental image (blue and green regions are used to compute the CNR). (b) Harmonic image (the yellow region is used to compute the RG). TRF estimated by (c) LASSO-fundamental, (d) LASSO-harmonic, (e) LASSO-sum, and (f) proposed method. All the TRF were restored using a PSF preestimated by homomorphic filtering. Note that all the images are shown in B-mode for better visualization and with 60-dB dynamic range.

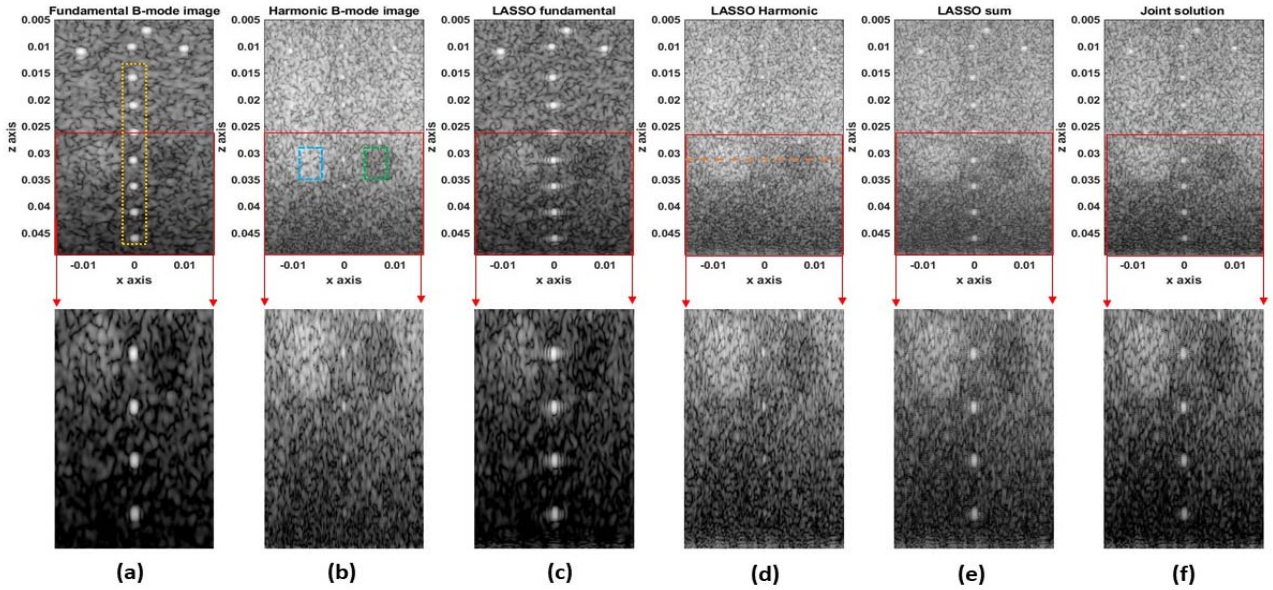

Fig. 10. Results on phantom data. (a) Fundamental image (yellow region is used to compute the RG). (b) Harmonic image (blue and green regions are used to compute the CNR). TRF estimated by (c) LASSO-fundamental, (d) LASSO-harmonic, (e) LASSO-sum, and (f) proposed method. All the TRF were restored using a PSF preestimated by homomorphic filtering. Note that all the images are shown in B-mode for better visualization and with 60-dB dynamic range.

and harmonic information. The experiments on carotid are following the same scheme as for the phantom. The results shown in Fig. 12 allow us to conclude that LASSO-sum and the proposed method, which use both fundamental and harmonic images, are able to gather useful information from both observations. In particular, they provide a spatial resolution similar to that of the harmonic image. However, harmonic images are highly attenuated with depth and, more generally, can be attenuated in any region corresponding to tissues with a low harmonic response. For those particular regions, the fundamental image plays an important role in order to compensate for this lack of information in the harmonic image. This effect can be appreciated in the zoomed regions shown in Fig. 12. Fig. 13 shows the profiles extracted from the TRF confirming these observations. The quantitative results are shown in Table VI, which highlights the interest of combining information from both fundamental and harmonic RF images. For this particular carotid experiment, one can observe that the harmonic image has a relatively strong amplitude for small depths, thus providing a very good spatial resolution and contrast, except for high depths. In particular, the CNR measured from the harmonic image is very high. However, one can observe that all the deconvolution methods allow the spatial resolution to be increased, highlighted by RG values always higher than 1 in Table VI. The proposed method reaches a compromise between spatial resolution (best compared with

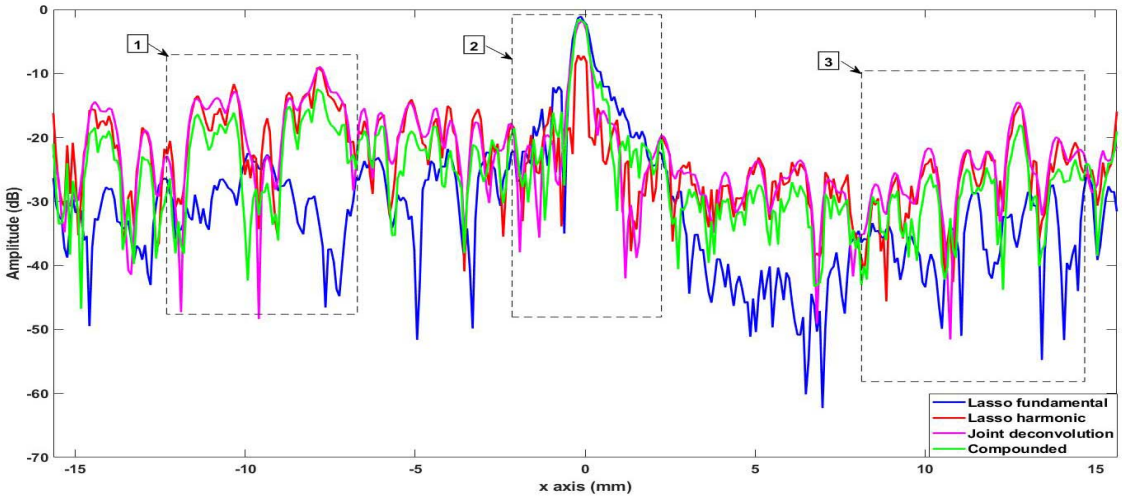

Fig. 11. Horizontal profile passing by the two cysts (regions 1 and 3) and the wire in between (region 2), the orange line in Fig.10(d).

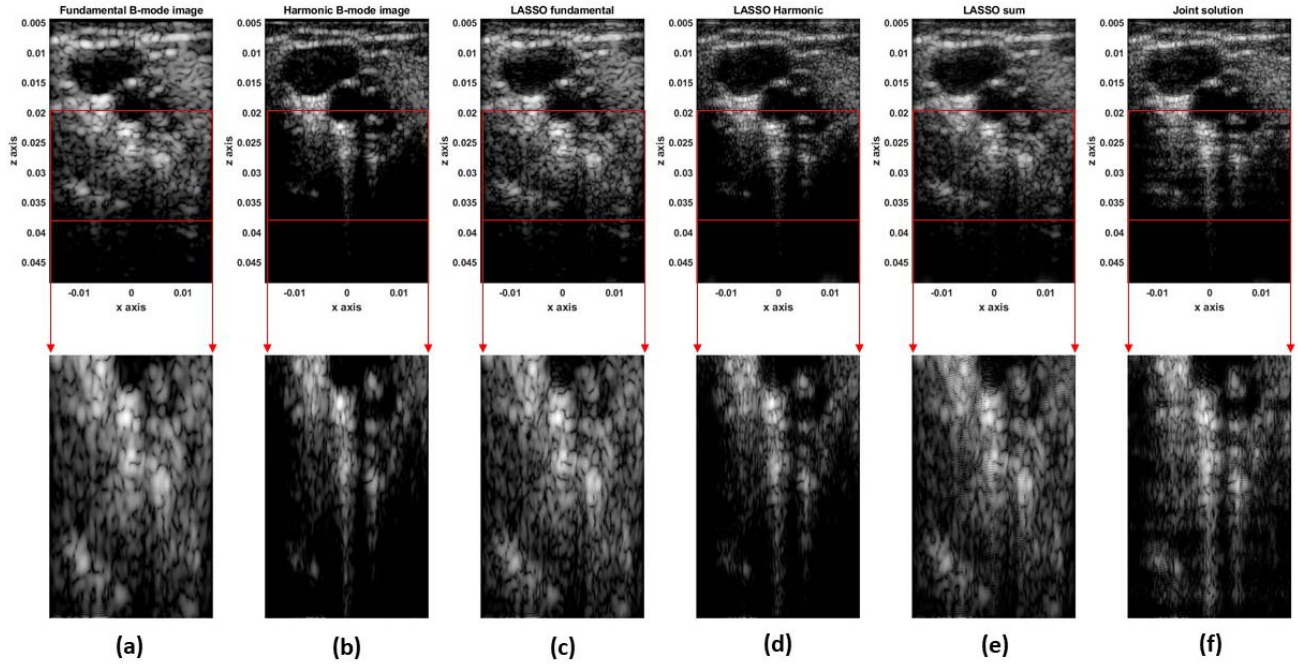

Fig. 12. Results on carotid data. (a) Fundamental image (green region is used to compute the RG). (b) Harmonic image (blue regions are used to compute the CNR). TRF estimated by (c) LASSO-fundamental, (d) LASSO-harmonic, (e) LASSO-sum, and (f) proposed method. All the TRF were restored using PSF pre-estimated by homomorphic filtering. Note that all the images are shown in B-mode for better visualization and with 60-dB dynamic range.

fundamental image and second best, hence very close to the best, compared with the harmonic image) and contrast (best CNR among all the deconvolution methods and close to the harmonic image).

The models used in this article for fundamental and harmonic components were linear based on the first-order Born approximation. If this assumption is valid for fundamental images in most practical applications, it is only valid for harmonic images acquired from media with low nonlinearities. To extend the proposed work to other applications than THI, such as perfusion techniques, nonlinear models should be considered to better fit the harmonic image formation model. The imaging formation models could also be improved by including spatially variant PSFs, adapted to various imaging strategies such as the classical focus scheme used in this work or synthetic strategies based on the plane or diverging waves. These more sophisticated models would certainly help to increase the accuracy of the image restoration process, e.g., by reducing the reverberation in the restored TRF images.

The blind deconvolution problem investigated in this work assumed that the noises of the fundamental and harmonic images are independent. Since the cross-correlation coefficient between the anechoic regions in the real data between the fundamental and harmonic images is close to zero, the latter assumption is considered fair enough in our application. Inverting the proposed image formation models

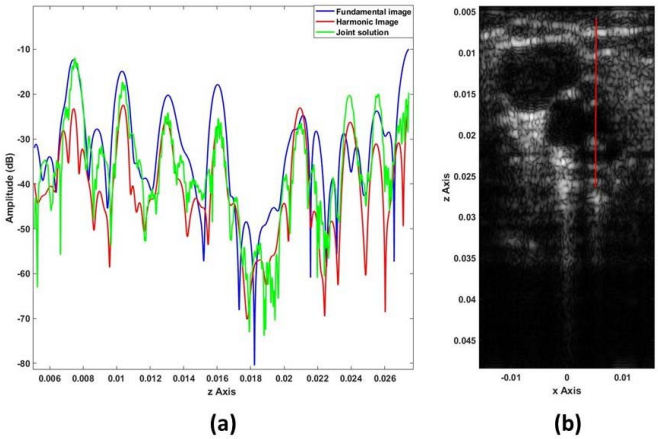

Fig. 13. (a) TRF profiles corresponding to the red line in (b).

TABLE VI
QUANTITATIVE RESULTS COMPUTED FROM THE IMAGES IN FIG. 12

	LASSO Fundamental	LASSO Harmonic	LASSO sum	Proposed method
CNR	9.832	**13.438**	8.38	12.069
RG/fund	2.226	5.308	8.513	**9.857**
RG/har	1.194	2.846	**5.882**	5.286

for the fundamental and harmonic images is an ill-posed inverse problem that requires regularization to stabilize the solution. In the present work, the regularization term was based on an ℓ_1-norm motivated by the assumption of a Laplacian-distributed TRF. However, other statistical models might be considered, e.g., using a generalized Gaussian distribution, which is more general than the Laplace distribution and was already shown to be a good candidate for US image restoration [8], [45]. It is interesting to mention here that the regularization parameters were fixed to their best values by cross validation. Thus, the hyperparameter μ balances the weight between the data fidelity term and the ℓ_1-norm regularization promoting sparsity. The hyperparameter β is proper to ADMM and allows the convergence of the algorithm to be monitored. It balances the importance of the linear constraint with respect to the data fidelity terms. Practically, the values of these hyperparameters were set to $\mu = 0.1$ and $\beta = 1$ for synthetic data and to $\mu = 0.05$ and $\beta = 0.5$ for the two real data sets (interestingly, it was not necessary to change these values from one real data set to another).

The execution time of the proposed deconvolution algorithm is about 1 min for one US image, on a standard 3.6-GHz Intel Core i7 with a straightforward MATLAB implementation. The current implementation[1] uses optimized ways of handling high-dimensional operators, by computing some of the steps in the Fourier domain as explained previously.

VI. CONCLUSION AND PERSPECTIVES

This article introduced a restoration method adapted to US imaging. Its main advantage compared to the state of the art is to consider two image formation models for fundamental and harmonic images, which are used jointly in the restoration process. This strategy combines the information from both RF images, in particular the good spatial resolution of harmonic data and the good SNR (especially for high depths) of fundamental data.

This work opens perspectives concerning various aspects of US image deconvolution, from the proposed image model to the resolution of the corresponding inverse problem.

An accurate knowledge of the PSF is an important prerequisite for any deconvolution method. In our work, the estimation of the PSFs was achieved in a preprocessing step, by homomorphic filtering. Considering other PSF estimation methods, in particular blind approaches that can estimate jointly the PSF and the high-resolution image, is clearly an interesting future work. Finally, ADMM was adopted in the proposed work to minimize the cost function resulting from the US deconvolution process. Despite its flexibility and interesting convergence properties, other optimization algorithms could offer interesting perspectives, especially for more complex image models, e.g., including nonlinear terms. Finally, a real-time implementation of the algorithm using parallel or GPU computing also represents an important perspective for clinical use.

[1]The MATLAB code is available at https://www.irit.fr/ Adrian.Basarab/codes.html

ACKNOWLEDGMENT

The authors would like to thank Dr. Alessandro Ramalli and Dr. Giulia Matrone for providing the experimental data used in this article to validate the proposed algorithm.

REFERENCES

[1] R. J. Eckersley, C. T. Chin, and P. N. Burns, "Optimising phase and amplitude modulation schemes for imaging microbubble contrast agents at low acoustic power," *Ultrasound Med. Biol.*, vol. 31, no. 2, pp. 213–219, Feb. 2005.
[2] A. Bouakaz and N. de Jong, "WFUMB safety symposium on echo-contrast agents: Nature and types of ultrasound contrast agents," *Ultrasound Med. Biol.*, vol. 33, no. 2, pp. 187–196, Feb. 2007.
[3] F. Tranquart, N. Grenier, V. Eder, and L. Pourcelot, "Clinical use of ultrasound tissue harmonic imaging," *Ultrasound Med. Biol.*, vol. 25, no. 6, pp. 889–894, Jul. 1999.
[4] J. D. Thomas and D. N. Rubin, "Tissue harmonic imaging: Why does it work?" *J. Amer. Soc. Echocardiograp.*, vol. 11, no. 8, pp. 803–808, Aug. 1998.
[5] D. H. Simpson, C. Ting Chin, and P. N. Burns, "Pulse inversion Doppler: A new method for detecting nonlinear echoes from microbubble contrast agents," *IEEE Trans. Ultrason., Ferroelectr., Freq. Control*, vol. 46, no. 2, pp. 372–382, Mar. 1999.
[6] M. Hourani, A. Basarab, D. Kouamé, J.-M. Girault, and J.-Y. Tourneret, "Restoration of ultrasonic images using non-linear system identification and deconvolution," in *Proc. Int. Symp. Biomed. Imag. (ISBI)*, Washington, DC, USA, Apr. 2018, pp. 1166–1169.
[7] P. Phukpattaranont and E. S. Ebbini, "Post-beamforming second-order volterra filter for pulse-echo ultrasonic imaging," *IEEE Trans. Ultrason., Ferroelectr., Freq. Control*, vol. 50, no. 8, pp. 987–1001, Aug. 2003.
[8] M. Alessandrini *et al.*, "A restoration framework for ultrasonic tissue characterization," *IEEE Trans. Ultrason., Ferroelectr., Freq. Control*, vol. 58, no. 11, pp. 2344–2360, Nov. 2011.
[9] T. Taxt, "Restoration of medical ultrasound images using two-dimensional homomorphic deconvolution," *IEEE Trans. Ultrason., Ferroelectr., Freq. Control*, vol. 42, no. 4, pp. 543–554, Jul. 1995.
[10] O. V. Michailovich and D. Adam, "A novel approach to the 2-D blind deconvolution problem in medical ultrasound," *IEEE Trans. Med. Imag.*, vol. 24, no. 1, pp. 86–104, Jan. 2005.
[11] U. R. Abeyratne, A. P. Petropulu, and J. M. Reid, "Higher order spectra based deconvolution of ultrasound images," *IEEE Trans. Ultrason., Ferroelectr., Freq. Control*, vol. 42, no. 6, pp. 1064–1075, Nov. 1995.

[12] C. Yu, C. Zhang, and L. Xie, "A blind deconvolution approach to ultrasound imaging," *IEEE Trans. Ultrason., Ferroelectr., Freq. Control*, vol. 59, no. 2, pp. 271–280, Feb. 2012.
[13] O. Michailovich, A. Basarab, and D. Kouamé, "Iterative reconstruction of medical ultrasound images using spectrally constrained phase updates," in *Proc. Int. Symp. Biomed. Imag. (ISBI)*, 2019, pp. 1765–1768.
[14] T. Taxt and R. Jirik, "Superresolution of ultrasound images using the first and second harmonic signal," *IEEE Trans. Ultrason., Ferroelectr., Freq. Control*, vol. 51, no. 2, pp. 163–175, Feb. 2004.
[15] A. Besson *et al.*, "A physical model of nonstationary blur in ultrasound imaging," *IEEE Trans. Comp. Img.*, vol. 5, no. 3, pp. 381–394, Feb. 2019.
[16] J. A. Jensen, "Field: A program for simulating ultrasound systems," in *Med. Biol. Eng. Comput.*, vol. 34, no. 1, pp. 351–353, 1996.
[17] J. Ng, R. Prager, N. Kingsbury, G. Treece, and A. Gee, "Modeling ultrasound imaging as a linear, shift-variant system," *IEEE Trans. Ultrason., Ferroelectr., Freq. Control*, vol. 53, no. 3, pp. 549–563, Mar. 2006.
[18] R. J. Zemp, C. K. Abbey, and M. F. Insana, "Linear system models for ultrasonic imaging: Application to signal statistics," *IEEE Trans. Ultrason., Ferroelectr., Freq. Control*, vol. 50, no. 6, pp. 642–654, Jun. 2003.
[19] J. A. Jensen, "A model for the propagation and scattering of ultrasound in tissue," *J. Acoust. Soc. Amer.*, vol. 89, no. 1, pp. 182–190, Jan. 1991.
[20] M. I. Florea, A. Basarab, D. Kouamé, and S. A. Vorobyov, "An axially variant kernel imaging model applied to ultrasound image reconstruction," *IEEE Signal Process. Lett.*, vol. 25, no. 7, pp. 961–965, Jul. 2018.
[21] O. V. Michailovich, "Non-stationary blind deconvolution of medical ultrasound scans," in *Proc. Med. Imag. Ultrason. Imag. Tomogr.*, Bellingham, WA, USA, Mar. 2017, Art. no. 101391C.
[22] J. Ardouin and A. Venetsanopoulos, "Modelling and restoration of ultrasonic phased-array B-scan images," *Ultrason. Imag.*, vol. 7, no. 3, pp. 321–344, Jul. 1985.
[23] J. G. Nagy and D. P. O'Leary, "Restoring images degraded by spatially variant blur," *SIAM J. Scientific Comput.*, vol. 19, no. 4, pp. 1063–1082, Jul. 1998.
[24] H. Gao *et al.*, "A fast convolution-based methodology to simulate 2-D/3-D cardiac ultrasound images," *IEEE Trans. Ultrason., Ferroelectr., Freq. Control*, vol. 56, no. 2, pp. 404–409, Feb. 2009.
[25] Z. Chen, A. Basarab, and D. Kouamé, "Compressive deconvolution in medical ultrasound imaging," *IEEE Trans. Med. Imag.*, vol. 35, no. 3, pp. 728–737, Mar. 2016.
[26] R. Morin, S. Bidon, A. Basarab, and D. Kouamé, "Semi-blind deconvolution for resolution enhancement in ultrasound imaging," in *Proc. IEEE Int. Conf. Image Process.*, Sep. 2013, pp. 1413–1417.
[27] O. Michailovich and A. Tannenbaum, "Blind deconvolution of medical ultrasound images: A parametric inverse filtering approach," *IEEE Trans. Image Process.*, vol. 16, no. 12, pp. 3005–3019, Dec. 2007.
[28] S. Boyd, N. Parikh, E. Chu, B. Peleato, and J. Eckstein, "Distributed optimization and statistical learning via the alternating direction method of multipliers," *Found. Trends Mach. Learn.*, vol. 3, no. 1, pp. 1–122, 2010.
[29] P. L. Combettes and J.-C. Pesquet, "Proximal splitting methods in signal processing," in *Fixed-Point Algorithms for Inverse Problems in Science and Engineering*. New York, NY, USA: Springer, 2011, pp. 185–212.
[30] A. Beck and M. Teboulle, "A fast iterative shrinkage-thresholding algorithm for linear inverse problems," *SIAM J. Imag. Sci.*, vol. 2, no. 1, pp. 183–202, Jan. 2009.
[31] D. Gabay and B. Mercier, "A dual algorithm for the solution of nonlinear variational problems via finite element approximation," *Comput. Math. Appl.*, vol. 2, no. 1, pp. 17–40, 1976.
[32] M. A. Figueiredo, J. M. Bioucas-Dias, and M. V. Afonso, "Fast frame-based image deconvolution using variable splitting and constrained optimization," in *Proc. IEEE/SP 15th Workshop Stat. Signal Process.*, Aug. 2009, pp. 109–112.
[33] M. V. Afonso, J. M. Bioucas-Dias, and M. A. T. Figueiredo, "An augmented lagrangian approach to the constrained optimization formulation of imaging inverse problems," *IEEE Trans. Image Process.*, vol. 20, no. 3, pp. 681–695, Mar. 2011.
[34] Z. Chen, A. Basarab, and D. Kouamé, "Reconstruction of enhanced ultrasound images from compressed measurements using simultaneous direction method of multipliers," *IEEE Trans. Ultrason., Ferroelectr., Freq. Control*, vol. 63, no. 10, pp. 1525–1534, Oct. 2016.
[35] R. Rangarajan, C. V. Krishnamurthy, and K. Balasubramaniam, "Ultrasonic imaging using a computed point spread function," *IEEE Trans. Ultrason., Ferroelectr., Freq. Control*, vol. 55, no. 2, pp. 451–464, Feb. 2008.
[36] A. V. Oppenheim, "Superposition in a class of nonlinear systems," Tech. Rep., 1965.
[37] T. Taxt, "Comparison of cepstrum-based methods for radial blind deconvolution of ultrasound images," *IEEE Trans. Ultrason., Ferroelectr., Freq. Control*, vol. 44, no. 3, pp. 666–674, May 1997.
[38] J. A. Jensen and S. Leeman, "Nonparametric estimation of ultrasound pulses," *IEEE Trans. Biomed. Eng.*, vol. 41, no. 10, pp. 929–936, Oct. 1994.
[39] H.-C. Shin *et al.*, "Sensitivity to point-spread function parameters in medical ultrasound image deconvolution," *Ultrasonics*, vol. 49, no. 3, pp. 344–357, Mar. 2009.
[40] G. Matrone, A. Ramalli, P. Tortoli, and G. Magenes, "Experimental evaluation of ultrasound higher-order harmonic imaging with filtered-delay multiply and sum (F-DMAS) non-linear beamforming," *Ultrasonics*, vol. 86, pp. 59–68, May 2018.
[41] S. Yoshifuku *et al.*, "Parametric harmonic-to-fundamental ratio contrast echocardiography: A novel approach to identification and accurate measurement of left ventricular area under variable levels of ultrasound signal attenuation," *Ultrasonics*, vol. 46, no. 2, pp. 109–118, May 2007.
[42] Z. Wang, A. C. Bovik, H. R. Sheikh, and E. P. Simoncelli, "Image quality assessment: From error visibility to structural similarity," *IEEE Trans. Image Process.*, vol. 13, no. 4, pp. 600–612, Apr. 2004.
[43] S.-J. Kim, K. Koh, M. Lustig, S. Boyd, and D. Gorinevsky, "An interior-point method for large-scale ℓ_1-regularized least squares," *IEEE J. Sel. Topics Signal Process.*, vol. 1, no. 4, pp. 606–617, Dec. 2007.
[44] F. Varray, O. Basset, P. Tortoli, and C. Cachard, "CREANUIS: A non-linear radiofrequency ultrasound image simulator," *Ultrasound Med. Biol.*, vol. 39, no. 10, pp. 1915–1924, Oct. 2013.
[45] N. Zhao, A. Basarab, D. Kouamé, and J.-Y. Tourneret, "Restoration of ultrasound images using a hierarchical Bayesian model with a generalized Gaussian prior," in *Proc. IEEE Int. Conf. Image Process. (ICIP)*, Oct. 2014, pp. 4577–4581.
[46] J. A. Jensen and P. Munk, "Computer phantoms for simulating ultrasound B-mode and CFM images," in *Acoustical Imaging*. Boston, MA, USA: Springer, 1997, pp. 75–80.

Mohamad Hourani (Student Member, IEEE) received the bachelor's degree in biomedical engineering from the Islamic University of Lebanon (IUL), Khalde, Lebanon, in 2016, and the master's degree in medical imaging and life physics from the Graduate School of Engineering (Polytech), University François Rabelais, Tours, France, in 2017. He is currently pursuing the Ph.D. degree with the National Institute of Polytechnic Toulouse (INPT-ENSEEIHT), Toulouse, France.

He is working in the Signal and Image Department, MINDS Team, 'Institue de Recherche en Informatique de Toulouse' (IRIT). He works mainly on the restoration of medical imaging, and more particularly, the restoration of medical ultrasound images by solving inverse problems and applying iterative algorithms for convex optimization and spectral analysis.

Adrian Basarab (Senior Member, IEEE) received the M.S. and Ph.D. degrees in signal and image processing from the National Institute for Applied Sciences, Lyon, France, in 2005 and 2008, respectively.

Since 2009 (respectively, 2016), he has been an Assistant (respectively, Associate) Professor with the University Paul Sabatier Toulouse 3, Toulouse, France, and a member of the IRIT Laboratory (UMR CNRS 5505). His research interests include medical imaging, and more particularly, inverse problems (deconvolution, super-resolution, compressive sampling, beamforming, image registration, and fusion) applied to ultrasound image formation, ultrasound elastography, cardiac ultrasound, quantitative acoustic microscopy, computed tomography, and magnetic resonance imaging.

Dr. Basarab is currently an Associate Editor of *Digital Signal Processing* and was a member of the French National Council of Universities Section 61—Computer sciences, Automatic Control and Signal Processing from 2010 to 2015. In 2017, he was a Co Guest Editor of the IEEE TUFFC Special Issue on "sparsity driven methods in medical ultrasound." Since 2018, he has been the Head of the "Computational Imaging and Vision" Group, IRIT Laboratory. Since 2019, he has been a member of the EURASIP Technical Area Committee Biomedical Image and Signal Analytics. Since 2020, he has been a member of the IEEE Ultrasonics Symposium TPC.

Denis Kouamé (Senior Member, IEEE) received the M.Sc., Ph.D., and Habilitation to Supervise Research Works (HDR) degrees in signal processing and medical ultrasound imaging from the University of Tours, Tours, France, in 1993, 1996, and 2004, respectively.

From 1996 to 1998, he was a Senior Engineer at GIP Tours, Tours. From 1998 to 2008, he was an Assistant then an Associate Professor at the University of Tours. He was the Head of the Signal and Image Processing Group, and then the Head of the Ultrasound Imaging Group, Ultrasound and Signal Laboratory, University of Tours, respectively, from 2000 to 2006 and from 2006 to 2008. From 2009 to 2015, he was the Head of health and information technology (HIT) strategic field at the Institut de Recherche en Informatique IRIT Laboratory, Toulouse, France. He currently leads the Signals and Image Department, IRIT. He has been a Professor in medical imaging and signal processing at the Paul Sabatier University of Toulouse, Toulouse, since 2008. His research interests cover the following areas: medical imaging, ultrasound imaging, high-resolution imaging, Doppler signal processing, and multidimensional biomedical signal and image analysis, including parametric modeling, spectral analysis, and application to flow estimation, sparse representation, and inverse problems.

Dr. Kouamé was invited for talks or in charge of different invited special sessions or tutorials at several IEEE conferences: ICASSP, ISBI, ISSPIT, and ICIP. He has served on several international conferences of technical program committees in signal, image processing, or medical imaging, and also chaired various sessions at different international conferences. He was/is/ invited for talks in different universities inside and outside France. He was/is involved, as a Principal Investigator or member, in different European or French research projects (ANR, FUI, and INSERM). He is an Associate Editor of the IEEE TRANSACTIONS ON ULTRASONICS FERROELECTRICS AND FREQUENCY CONTROL and IEEE TRANSACTIONS ON IMAGE PROCESSING.

Jean-Yves Tourneret (Fellow, IEEE) received the Ingénieur degree in electrical engineering from the École Nationale Supérieure d'Electronique, d'Electrotechnique, d'Informatique, d'Hydraulique et des Télécommunications (ENSEEIHT) de Toulouse, Toulouse, France, in 1989, and the Ph.D. degree from the National Polytechnic Institute, Toulouse, in 1992.

He is currently a Professor with the University of Toulouse (ENSEEIHT) and a member of the IRIT Laboratory (UMR 5505 of the CNRS). His research activities are centered around statistical signal and image processing with a particular interest to Bayesian and Markov chain Monte Carlo (MCMC) methods. He has been involved in the organization of several conferences, including the European Conference on Signal Processing EUSIPCO'02 (Program Chair), the international conference ICASSP'06 (plenaries), the statistical signal processing workshop SSP'12 (international liaisons), the International Workshop on Computational Advances in Multi-Sensor Adaptive Processing CAMSAP 2013 (local arrangements), the statistical signal processing workshop SSP'2014 (special sessions), and the workshop on machine learning for signal processing MLSP'2014 (special sessions). He has been the General Chair of the CIMI workshop on optimization and statistics in image processing hold in Toulouse in 2013 (with F. Malgouyres and D. Kouamé) and of the International Workshop on Computational Advances in Multi-Sensor Adaptive Processing (CAMSAP) in 2015 (with P. Djuric) and in 2019 (with D. Brie). He has been a member of different technical committees, including the Signal Processing Theory and Methods (SPTM) Committee of the IEEE Signal Processing Society from 2001 to 2007 and from 2010 to 2015 and the EURASIP SAT Committee on Theoretical and Methodological Trends in Signal Processing from 2015 to 2019. In 2019, he joined the board of directors of EURASIP. He was an Associate Editor of the IEEE TRANSACTIONS ON SIGNAL PROCESSING from 2008 to 2011and from 2015 to 2019 and the *EURASIP Journal on Advances in Signal Processing* from 2013 to 2019.